Surface Science 743 (2024) 122453

Contents lists available at ScienceDirect

Surface Science

journal homepage: www.elsevier.com/locate/susc

Reactivity of a model SCILL: Influence of co-adsorbed $[C_2C_1Im][OTf]$ on the dehydrogenation of dimethylamine on Pt(111)

Roman Eschenbacher [a], Julien Steffen [b,e], Karl Farrugia [a], Nicola Taccardi [c], Peter Wasserscheid [c,d], Andreas Görling [b,e], Jörg Libuda [a,*]

[a] Interface Research and Catalysis, ECRC, Friedrich-Alexander-Universität Erlangen-Nürnberg, Egerlandstraße 3, Erlangen 91058, Federal Republic of Germany
[b] Chair of Theoretical Chemistry, Friedrich-Alexander-Universität Erlangen-Nürnberg, Egerlandstrasse 3, Erlangen 91058, Federal Republic of Germany
[c] Institute of Chemical Reaction Engineering, Friedrich-Alexander-Universität Erlangen-Nürnberg, Egerlandstraße 3, Erlangen D-91058, Federal Republic of Germany
[d] Forschungszentrum Jülich GmbH, Helmholtz Institute Erlangen-Nürnberg for Renewable Energy, Egerlandstraße 3, Erlangen D-91058, Federal Republic of Germany
[e] Erlangen National High Performance Computing Center (NHR@FAU), Martensstrasse1, Erlangen D-91058, Federal Republic of Germany

ARTICLE INFO

Keywords:
Ionic liquid
SCILL
Infrared spectroscopy
Dehydrogenation
Catalysis

ABSTRACT

Solid catalysts with ionic liquid layers (SCILLs) are heterogeneous catalysts whose selectivity is significantly improved by the application of a thin coating of an ionic liquid (IL). In this work, we studied the influence of the IL 1-ethyl-3-methyl-imidazolium-trifluormethansulfonate ($[C_2C_1Im][OTf]$) on the dehydrogenation of dimethylamine (DMA) on Pt(111) by surface science experiments under ultrahigh vacuum (UHV) conditions. We investigated the growth, thermal stability, and the dehydrogenation reaction of DMA on Pt(111) both in the presence and absence of $[C_2C_1Im][OTf]$ by time-resolved and temperature-programmed infrared reflection absorption spectroscopy (IRAS) and density functional theory (DFT). We found that pre-adsorbed DMA has a strong influence on the interaction of $[C_2C_1Im][OTf]$ with the Pt surface. The competition for the same adsorption sites leads to changes in the binding motif and binding angles of the IL. In the presence of the IL, the reaction temperature of DMA is shifted to higher temperature due to the same competition and blocking effects. Thus, the IL leads to an enhanced stability of DMA on the surface and influences the product spectrum of the dehydrogenation reaction at higher temperature.

1. Introduction

In the solid catalysts with ionic liquid layer (SCILL) concept, a conventional heterogeneous supported catalyst is coated with a thin film of an ionic liquid (IL) [1–6]. The IL serves as a catalytic modifier and improves the selectivity of the catalyst [2,3,7]. ILs are low melting salts consisting of organic cations and anions. They are extremely versatile as a large number of ions can be combined, which allows us to tailor the physicochemical properties in a task-specific manner [8–12]. ILs are used in numerous applications, e.g. in catalysis [2,13,14], energy conversion [15–20], sensors [21], and actuators [22,23]. SCILL catalysts are already used at the industrial scale, in particular in case of hydrogenation reactions [5,24–26].

In SCILL systems, the active metal sites are selectively modified by the adsorption of IL ions [1,26–28]. To design such systems at a knowledge-driven basis, it is essential to understand this interaction at the microscopic level. Surface science experiments in ultrahigh vacuum (UHV) can provide very detailed information about the metal-IL interactions [4,7,29,30].

Due to the exceptionally low vapor pressure of ILs, stable IL films can be deposited onto atomically defined surfaces through physical vapor deposition (PVD) in UHV [4,30–33]. This enables surface science experiments which reveal detailed information on the IL/catalyst interaction, for example on the wetting characteristics and on the orientation of IL ions at the interface [29,34–37]. A widely explored area for SCILL systems are hydrogenation reactions [5,6,38–41], where SCILLs enable improved selectivity. In contrast, dehydrogenation reactions with SCILLs have rarely been studied.

In previous surface science studies, we have investigated the interaction of 1-ethyl-3-methyl-imidazolium-trifluormethansulfonat ($[C_2C_1Im][OTf]$) on various substrates, e.g. Pd(111) [3,42], Au(111) [43], and Al_2O_3 [44] by infrared reflection absorption spectroscopy (IRAS). On Pt(111), $[C_2C_1Im][OTf]$ was also investigated under potential control [45,46].

* Corresponding author.
E-mail address: joerg.libuda@fau.de (J. Libuda).

https://doi.org/10.1016/j.susc.2024.122453
Received 4 December 2023; Received in revised form 29 January 2024; Accepted 31 January 2024
Available online 3 February 2024

In this work, we focus on the interaction of $[C_2C_1Im][OTf]$ with Pt(111) and the effect of the IL on a dehydrogenation reaction. We chose the dehydrogenation of dimethylamine (DMA) as a test reaction. The surface chemistry of DMA on Pt(111) has already been studied in detail by Trenary and coworkers [47,48]. The dehydrogenation occurs in a temperature regime in which the IL wetting layer resides on the surface under UHV conditions. As a result, we expect to be able to identify clear effects of the co-adsorbed IL on the reaction mechanism and kinetics. Indeed, we found that DMA and IL compete for adsorption sites on Pt(111), forming mixed co-adsorbate layers. The co-adsorbed IL blocks some active platinum sites and, thus, stabilizes the DMA up to higher temperature.

2. Methods

2.1. Experimental setup

The IRAS experiments were performed in a UHV IRAS system with a base pressure of 1×10^{-10} mbar. The setup consists of various preparation and characterization tools which are necessary to prepare and investigate thin films. The setup is equipped with a vacuum Fourier-transform infrared (FTIR) spectrometer (Bruker Vertex 80v). A detailed description of the setup is given in the literature [49].

2.2. Preparation of the Pt(111) single crystal

The Pt(111) single crystal (MaTecK) was cleaned by several cycles of Ar^+ sputtering (1.5 keV, 300 K, 30 min, 8×10^{-5} mbar, Linde, purity 99.9999 %). To this end, the sample was annealed at 1000 K for 10 min both in UHV and in O_2 atmosphere (4×10^{-7} mbar, Linde, purity 99.999 %). A subsequent heating step to 1100 K in UHV was applied to remove residual O_2. The cleanliness of the sample was checked by IRAS *via* adsorption of CO at 300 K (1×10^{-6} mbar, Westfalen 99.97 %). Traces of carbonyls were removed from the supplied CO *via* a homebuilt liquid nitrogen trap. After stepwise CO adsorption, the sample was cleaned again by a sputtering and annealing cycle.

2.3. Deposition of dimethylamine

Dimethylamine (abcr GmbH, 99 %) was dosed *via* a fine leak valve with a pressure of 1.33×10^{-7} mbar resulting in a deposition rate of 0.1 L/s. The fine leak valve was separated from the chamber *via* a gate valve with a separate high vacuum line.

2.4. Deposition of $[C_2C_1Im][OTf]$

IL was deposited *via* PVD by evaporation from a home-built Knudsen cell in form of a glass crucible loaded with $[C_2C_1Im][OTf]$ until a thin

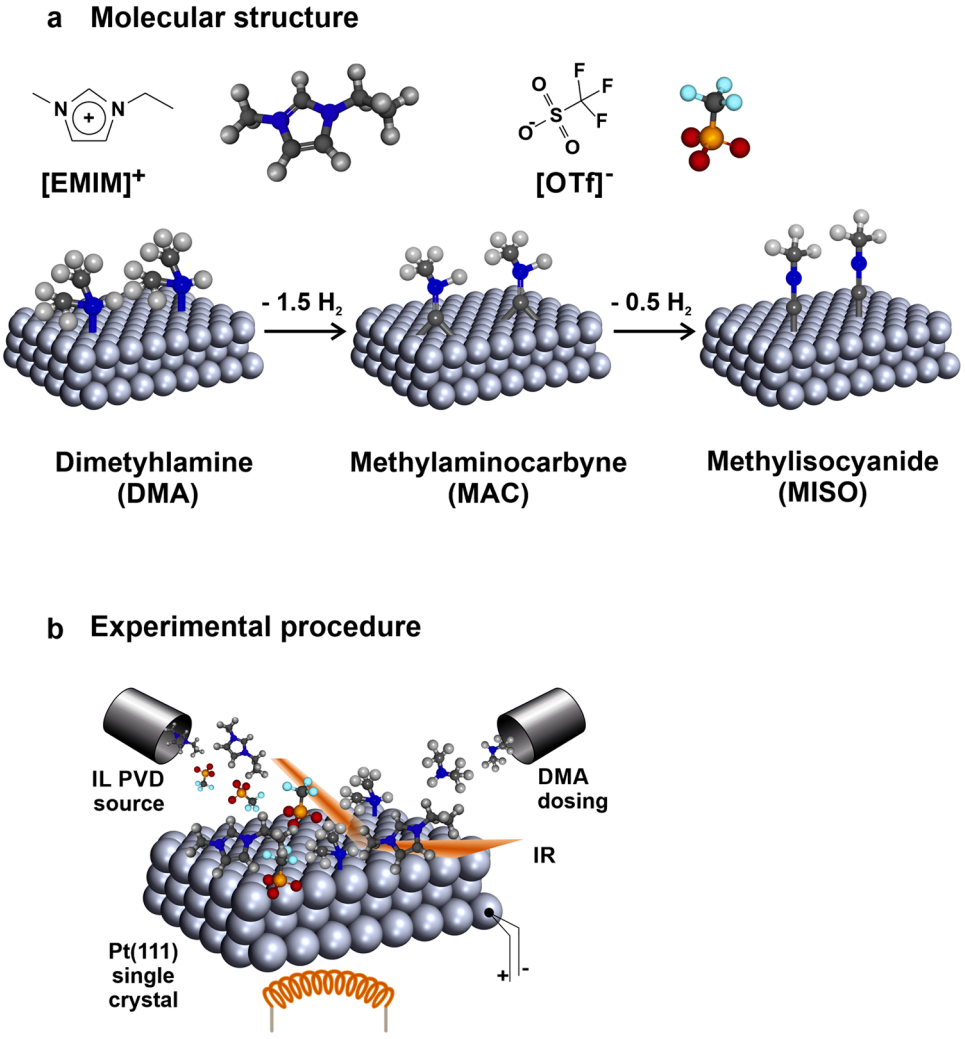

Fig. 1. Model systems investigated: (a) top: molecular structures of the IL cation $[C_2C_1Im]^+$ and the anion $[OTf]^-$; bottom: partial dehydrogenation reactions of dimethylamine to methylaminocarbyne (MAC) and methylisocyanide (MISO) with the extraction of 1.5 H_2 and 0.5 H_2 on Pt(111); (b) schematic sketch of the *in situ* IRAS setup.

film (thickness ~ 1 ML) was prepared (see Fig. 1). The evaporator was pumped through a separate high vacuum line and baked for 24 h at moderate temperatures to aid degassing of the IL prior the experiments. For deposition, the IL was preheated to 400 K. The film growth was monitored *via* time-resolved IRAS where one spectrum was measured every minute with a constant deposition rate. We used the following IRAS parameters: scanning time of 0.9 min/spectrum; background spectrum of 10 min; data measured from 4000 to 600 cm^{-1}; MIR source; KBr beam splitter; LN-MCT narrow detector; 40 kHz scanner velocity.

2.5. Temperature-programmed IRAS (TP-IRAS)

IR spectra were acquired while heating the samples with a linear heating ramp from 120 to 700 K (1 spectrum/min, heating rate of 2 K/min) in UHV. The spectra were referred to the background of the clean surface at 120 K.

2.6. Density functional theory (DFT) calculations

Periodic DFT modeling of the system was carried out with the VASP code, in which a plane wave basis set is used for the description of the valence electrons and combined with the projector augmented wave (PAW) method for the representation of the atomic cores [50–52]. The kinetic energy cutoff was chosen to be 600 eV for metal surface slab and adsorbate optimizations, exchange correlation effects were treated with the PBE functional [53]. The DFT-D3 correction with Becke–Johnson damping was used for the better description of dispersion interactions in the case of adsorbate optimizations [54,55]. The Pt(111) surface was modeled as a 4 × 4 surface slab with five atom layers deep, where the lowest two layers were held fixed at bulk configuration during geometry relaxations. A vacuum separation of 20 Å was added between the periodic images of the Pt surface in order to ensure enough space between them also in the case of added adsorbates. Brillouin zone sampling was done with a Γ-containing 4 × 4 × 1 k-point mesh [56]. A Methfessel-Paxton scheme with a broadening of 0.15 eV was applied to smear the electronic states. The geometry of the model surface was relaxed until all gradient components were below 0.01 eV/Å, the three adsorbate molecules (dimethylamine, methylaminocarbyne and methylisocyanide) were placed at different positions on the surface and the whole system was reoptimized until all gradient components were below 0.02 eV/Å. For the vacuum calculations, the molecules were optimized in an empty unit cell of the same size as for the adsorbate optimizations, and the resulting energy was added to the energy of the clean Pt(111) surface slab. All methylaminocarbyne calculations were done spin-polarized. Numerical frequencies were calculated for the optimized adsorbates, where only the atoms of the adsorbate molecules were activated for numerical displacement. The peaks in the eigenvalue spectrum obtained from the harmonic approximation were broadened with the program Molden; the halfwidths were 10 cm^{-1}. The metal surface selection rule is considered, since dipole corrections along the z-axis were applied in the VASP calculations. No energy or frequency shifts were applied to the calculated IR spectra.

2.7. Synthesis of 1-ethyl-3-methylimidazolium trifluoromethanesulfonate [C_2C_1Im][OTf]

N-methylimidazole and ethyl trifluoromethanesulfonate were purchased from Aldrich. N-methylimidazole was distilled prior usage. ^1H NMR measurements were carried out using a Jeol ECX 400 MHz spectrometer and d_6-DMSO as solvent. For the synthesis of 1-ethyl-3-methylimidazolium triflate, 74.720 g (0.419 mol, 1.01 equiv.) of ethyl trifluoromethanesulfonate was dropwise added to 34.195 g (0.417 mol) of N-methylimidazole from Aldrich under argon atmosphere at 0 °C. After addition, the reaction mixture was allowed to warm up to room temperature and stirred overnight. The reaction was monitored by ^1H NMR spectroscopy. The product was obtained in quantitative yield as a clear colorless liquid. The product was cleaned under vacuum (about 10^{-2} mbar) at 60 °C for 16 h.

3. Results and discussion

3.1. Dimethylamine (DMA) on Pt(111) at 120 K

First, we investigate the deposition of the dimethylamine (DMA) (Fig. 2). We recorded the IRA spectra (bottom three) which were acquired at ~ 0.4 L (submonolayer coverage), at ~ 1 L (monolayer coverage), and at ~ 2 L (multilayer coverage). At submonolayer coverage, bands are observed at 3000–2750 cm^{-1}, 1475 cm^{-1}, 1186 cm^{-1}, 990 cm^{-1} and 899 cm^{-1}, which are assigned to the symmetric and asymmetric ν(CH) vibrations, δ(CH_3), ν(C-N-C)$_s$, δ(CH_3) and δ(N-H) modes, respectively. With increasing coverage (~ 1 L), an additional band forms at 1140 cm^{-1}, assigned to δ(CH_3). In the multilayer region (~ 2 L), a broad band 3277 cm^{-1} is observed, which is assigned to the ν(NH) vibration. In IRA spectroscopy, both the reorientation of adsorbates on the surface and specific adsorption motifs lead to changes in band intensities. Intensity changes are governed by the metal-surface selection rule (MSSR) [57], which states that only those modes which have a perpendicular component of the dynamic dipole moment are observed. The parallel component of the dynamic dipole moment is screened by the metal surface. Bands such as the ν(C-N-C)$_s$ and ν(CH) vibrations give rise to substantial signals even in the submonolayer coverage. The δ(N-H) band together with the absence of the ν(NH) vibration in the (sub-)monolayer suggests that the N-H bond is oriented parallel to the Pt(111) surface or that the H is strongly interacting with the surface. With increasing coverage, these specific signals become less dominant as compared to other signals indicating a more random orientation above ~ 1 L. A small amount of CO adsorption from the background is observable at a coverage of less than 0.02 ML. Since this fraction is very small, we assume that these traces will have no influence on the DMA/MAC adsorption and the reaction behavior.

In the next step, we compare the IRAS data with the DFT calculations (top three spectra). In the DFT calculations, a single spectrum was computed for each adsorption motif (see the experimental section for more information). This allows us to verify whether non-dissociative adsorption is possible and provides insights on the orientation of DMA on Pt(111). The relative adsorption energies are provided together with the molecular structures in Fig. 2. In structure 1, the DMA is bound with the nitrogen atom in an atop position. This is the only structure which is predicted to show a ν(NH) mode. Since this feature is not present in the monolayer, we conclude that this adsorption motif is not relevant at low coverage. Adsorption structure 2 is predicted to be the least favorable motif with the nitrogen bound in a displaced atop position. Structure 3 is predicted to show the highest adsorption energy with DMA bound in a atop position. The calculated spectra for both structures 2 and 3 are consistent with the measured data. The last adsorption motif (structure 4) is predicted to show an IR spectrum which does not agree well with the experimental data. Because of the energetic preference, we propose that structure 3 is the most common one on the surface. However, there are several additional bands observed in the experimental spectra, which suggests the coexistence of different adsorption motifs at low temperature. In summary, we conclude that DMA adsorbs non-dissociatively on Pt(111) at 120 K. The DMA binds *via* the nitrogen lone electron pair at an atop position to a Pt surface atom. The low mobility of DMA at 120 K may explain why adsorption motifs with lower adsorption energy are also observed in the IRAS data.

3.2. Methylaminocarbyne (MAC) on Pt(111) at 300 K

Next, we analyzed the adsorption of DMA on a clean Pt(111) surface at room temperature (Fig. 3). At this temperature, the IRA spectra are drastically different from those at 120 K. At low coverage (~ 0.4 L), bands are observed at 2918 cm^{-1}, 1466 cm^{-1}, 1402 cm^{-1}, 1290 cm^{-1}

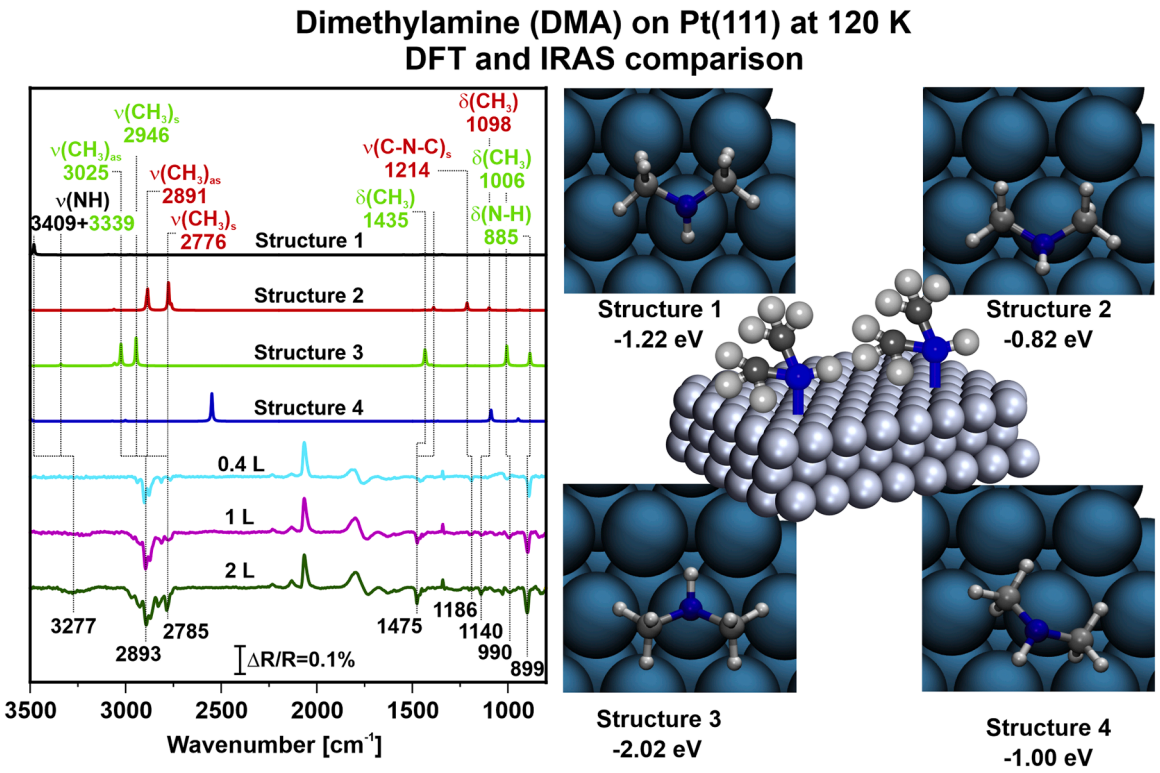

Fig. 2. Investigation of dimethylamine (DMA) on Pt(111); left plot: DFT spectra of DMA at different adsorption motifs (top) and IRA spectra of different DMA coverages at 120 K (bottom); right: different calculated adsorption motifs with their relative adsorption energies.

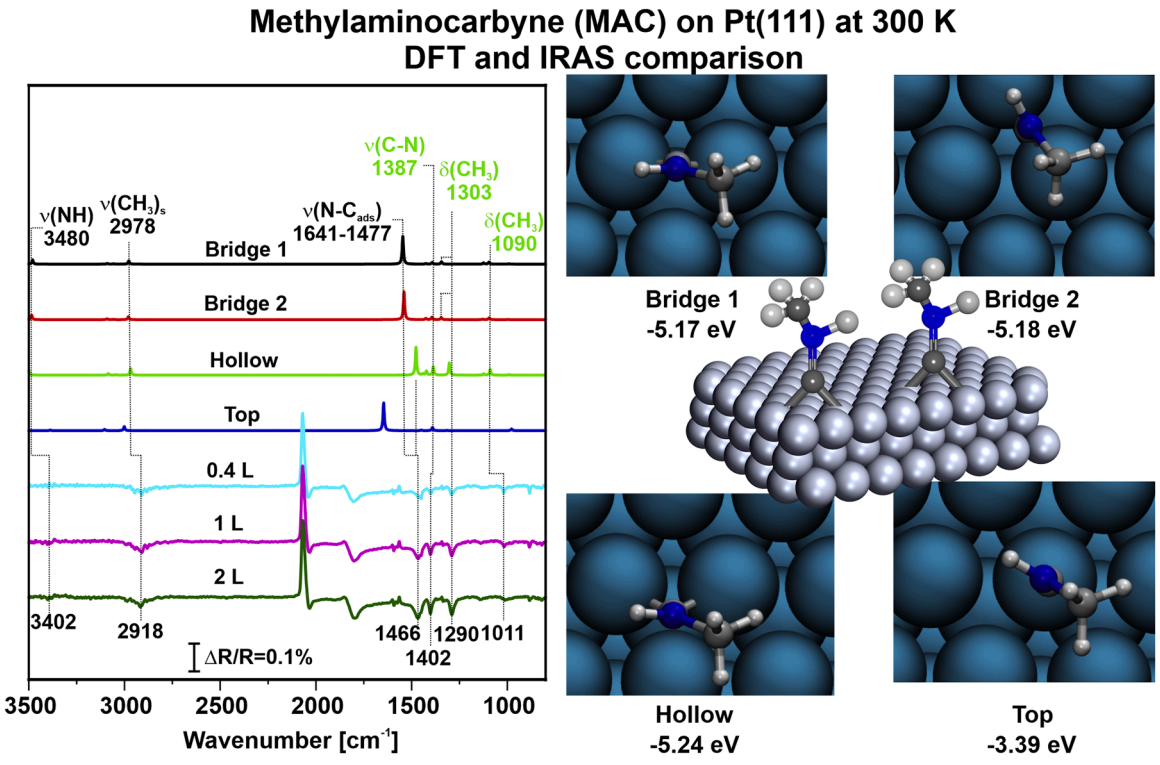

Fig. 3. Investigation of methylaminocarbyne (MAC) on Pt(111); left plot: DFT spectra of MAC at different adsorption motifs (top) and IRA spectra of different MAC coverages at 300 K (bottom); right: different calculated adsorption motifs with their relative adsorption energies.

and 1011 cm^{-1}. We assign these signals to the $\nu(CH_3)_s$, $\nu(N\text{-}C_{ads})$, $\nu(C\text{-}N)$, $\delta(CH_3)$ and $\delta(CH_3)$ modes, respectively. With increasing coverage, all bands grow linearly, indicating no specific adsorption behavior. In the multilayer regime at ~ 2 L, an additional small and broad band can be observed at 3402 cm^{-1}, which is assigned to the $\nu(NH)$ mode. The appearance of the band at 1466 cm^{-1} indicates the formation of a

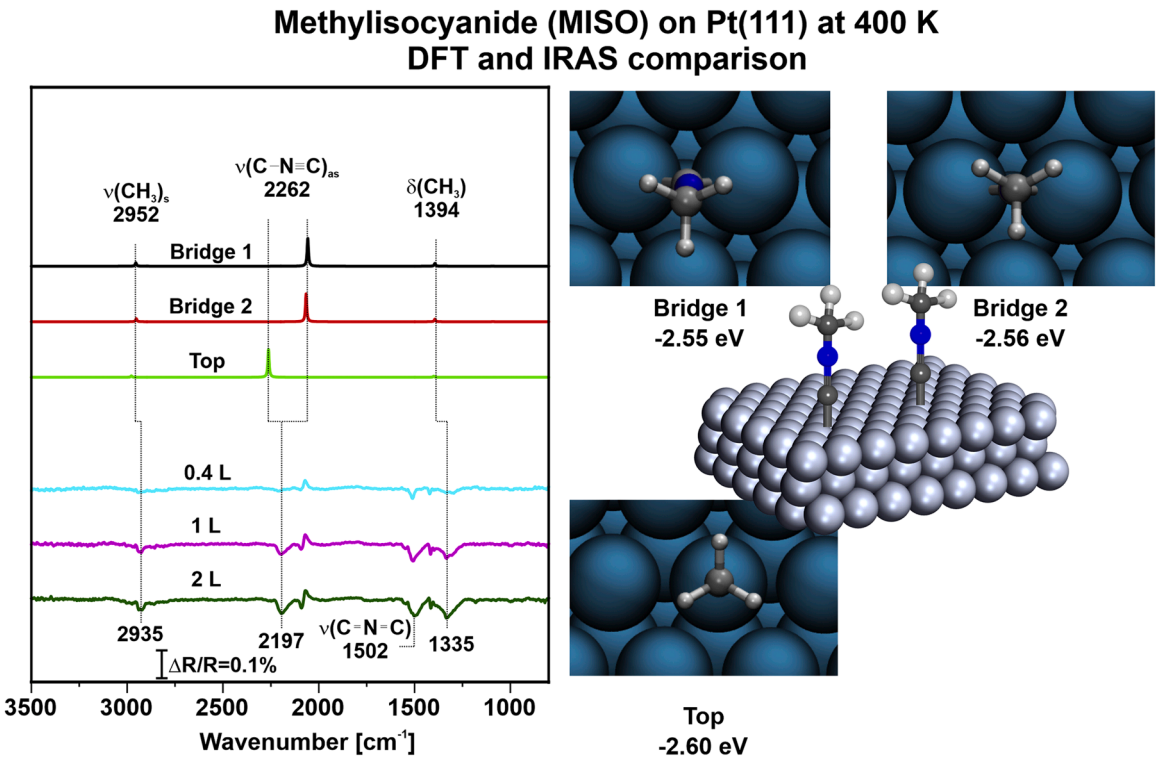

Fig. 4. Investigation of methylisocyanide (MISO) on Pt(111); left plot: DFT spectra of MISO at different adsorption motifs (top) and IRA spectra of different MISO coverages at 400 K; right: different calculated adsorption motifs with their relative adsorption energies.

reaction product. Mudiyanselage et al. previously proposed dehydrogenation and the formation of methylaminocarbyne (MAC) [48]. The DFT spectra for MAC agree well with the measured ones (see Fig. 3). We conclude that the DMA undergoes partial dehydrogenation and formation of MAC. Another indicator for the partial dehydrogenation is the shift of the ν(NH) vibration from 3277 cm^{-1} (DMA) to 3402 cm^{-1} (MAC), since the nitrogen of the NH group is no longer in direct contact with the platinum surface and with other DMA molecules.

We investigated the different adsorption motifs of MAC by DFT and compared the simulated IR spectra to the experimental ones (see Fig. 3). The least favorable structure is the adsorption in atop position and the simulated IR spectrum is also clearly different from experimental one. Adsorption in bridge and hollow positions are predicted to show very similar adsorption energy and the calculated IR spectra are all compatible with the experimental one. We suggest that MAC can adsorb in bridge and hollow positions on the Pt(111).

3.3. Methylisocyanide (MISO) on Pt(111) at 400 K

In the next step, we dosed DMA at elevated temperatures. At 400 K, bands are observed at 2935 cm^{-1}, 2197 cm^{-1}, 1502 cm^{-1} and 1335 cm^{-1} at a coverage of ~ 0.4 L (see Fig. 4). We assign these bands to the

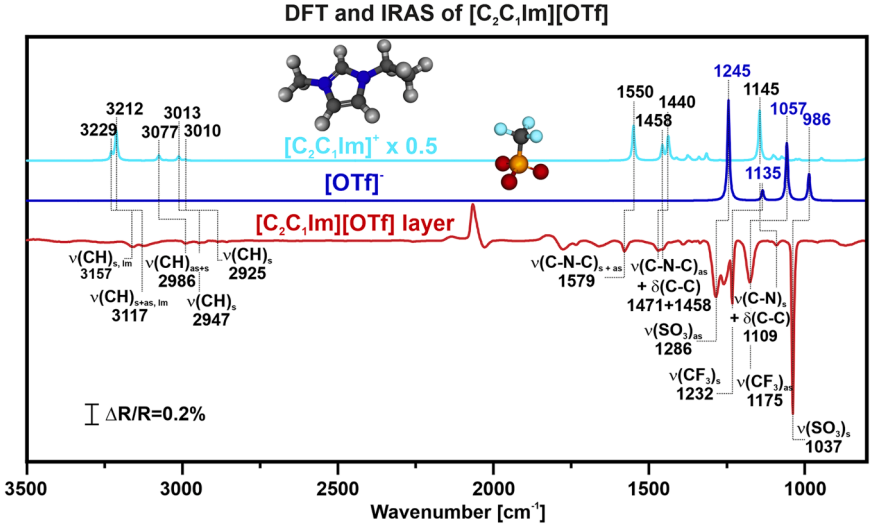

Fig. 5. DFT of the $[C_2C_1Im]^+$ cation (light blue) and the $[OTf]^-$ anion (deep blue) and multilayer IRA spectra (red) of $[C_2C_1Im][OTf]$ on Pt(111) at 120 K. The most prominent bands are labelled and assigned according to DFT calculations (For interpretation of the references to color in this figure legend, the reader is referred to the web version of this article.).

Table 1
DFT Peak positions and IL peak assignment based on $[C_2C_1Im][OTf]$ multilayer spectrum on Pt(111).

DFT peak position	IRAS peak position	Assignment [37,58,62,63]
1245 cm^{-1}	1286 cm^{-1}	$\nu(SO_2)_{as}$
1135 cm^{-1}	1232 cm^{-1}	$\nu(CF_3)_s$
1057 cm^{-1}	1175 cm^{-1}	$\nu(CF_3)_{as}$
986 cm^{-1}	1037 cm^{-1}	$\nu(SO_2)_s$
3229 cm^{-1}	3157 cm^{-1}	$\nu(CH)_{s,\ Im}$
3213 cm^{-1}	3117 cm^{-1}	$\nu(CH)_{s+as,\ Im}$
3013 cm^{-1}	2986 cm^{-1}	$\nu(CH)_{s+as}$
3010 cm^{-1}	2947 cm^{-1}	$\nu(CH)_s$
2991 cm^{-1}	2925 cm^{-1}	$\nu(CH)_s$
1550 cm^{-1}	1579 cm^{-1}	$\nu(C\text{-}N\text{-}C)_{s+as}$
1438 + 1458 cm^{-1}	1471 + 1458 cm^{-1}	$\nu(C\text{-}N\text{-}C)_{as} + \delta(C\text{-}C)$
1145 cm^{-1}	1109 cm^{-1}	$\nu(C\text{-}N)_s + \delta(C\text{-}C)$

$\nu(CH_3)_s$, $\nu(C\text{-}N{\equiv}C)_{as}$, $\nu(C{=}N{=}C)$ and $\delta(CH_3)$ modes, respectively. With increasing coverage, all bands increase linearly in intensity. This indicates layer growth without substantial reorientation. The band at 2197 cm^{-1} is characteristic for the $\nu(C\text{-}N{\equiv}C)_{as}$ mode with a CN triple bond that can be used as an indicator for the formation of methylisocyanide (MISO), as previously described in the literature [48]. It has been suggested that the band at 1502 cm^{-1} can be assigned to formimidine [48], an intermediate of the conversion of MAC to MISO. The DFT calculations for the adsorption of MISO on Pt(111) are shown in Fig. 4. It is predicted that adsorption of MISO in atop and bridge position occurs with similar adsorption energies. Moreover, the calculated positions of the IR bands are very close to each other. Therefore, it is not possible to distinguish between the adsorption motifs experimentally.

3.4. IR spectrum of $[C_2C_1Im][OTf]$

Next, we examined the IR spectra of $[C_2C_1Im][OTf]$ deposited by PVD on Pt(111). In Fig. 5, we compare the multilayer spectra (~ 2 monolayers (ML), where 1 ML is defined as a closed double layer of chemisorbed ion pairs) [58]. The band assignments in Table 1 are based on DFT data and previous IRAS studies on other metal supports [3,42,44,45,59]. Note that in IRAS measurements, only the components of the dynamic dipole moments of the vibrational modes perpendicular to the surface give rise to an absorption signal (MSSR rule) [57]. The IRA Spectra agree very well with the DFT spectra indicating the IL film is deposited on the surface without any indication for decomposition.

3.5. Growth of $[C_2C_1Im][OTf]$ on Pt(111)

Now, we focus on the IL layers on clean Pt(111). In Fig. 6, we show IR data measured during the deposition of the IL molecules by PVD both at room temperature (300 K) and at 120 K. Since the spectrum of the multilayer was discussed above, we first focus on the monolayer region only. The growth behavior of the IL at room temperature has already been described in the literature for Au(111) [43], Pd(111) [3,42] and Al_2O_3 [44]. Based on these findings, we first consider the growth at 300 K (Fig. 6b) and assign the bands accordingly. The bands marked in green are symmetric vibrations; the asymmetric ones are marked in light blue.

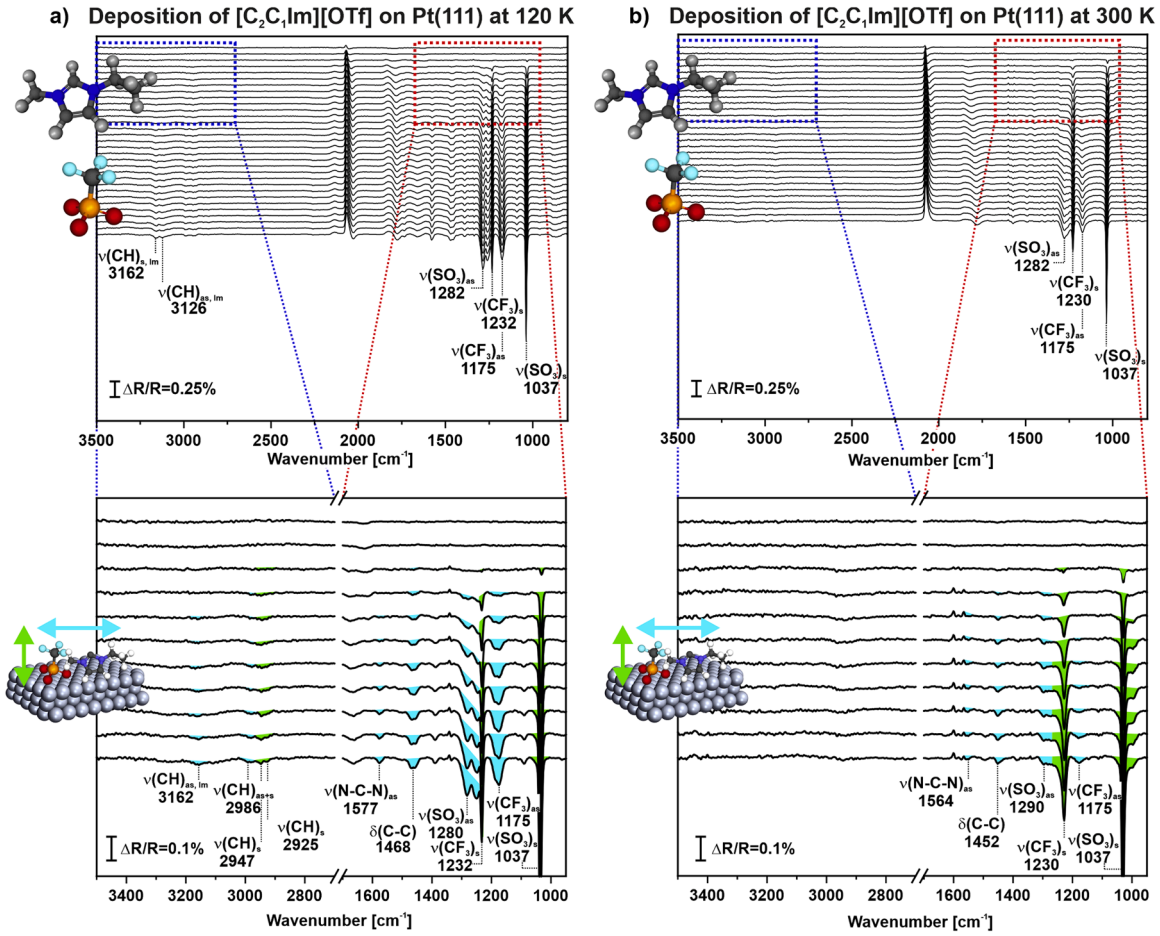

Fig. 6. Time resolved IRAS of the film growth of $[C_2C_1Im][OTf]$ on Pt(111) at (a) 300 K and (b) 120 K. Zoomed in parts from 3500 cm^{-1} to 2700 cm^{-1} (blue) and 1700 cm^{-1} to 900 cm^{-1} (red) for the investigation of (sub-)monolayer growth. The bands marked in green are symmetric vibrations; the asymmetric ones are marked in light blue (For interpretation of the references to color in this figure legend, the reader is referred to the web version of this article.).

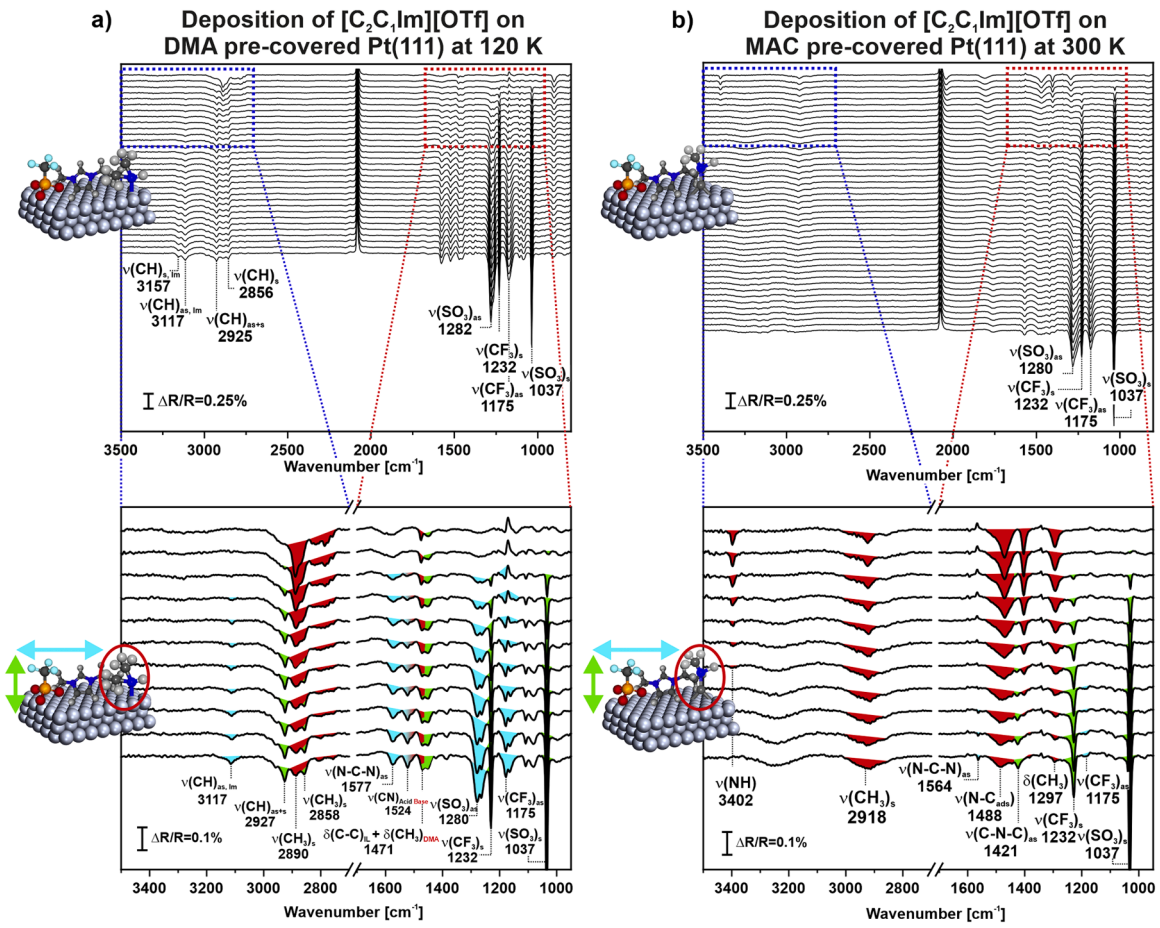

Fig. 7. Time resolved IRAS of the film growth of $[C_2C_1Im][OTf]$ on a DMA pre-adsorbed (~ 2 L) Pt(111) at a) 120 K and b) 300 K. Zoomed in parts from 3500 cm^{-1} to 2700 cm^{-1} (blue) and 1700 cm^{-1} to 900 cm^{-1} (red) to investigate the (sub-)monolayer growth. DMA/MAC bands are marked in red, symmetric $[C_2C_1Im][OTf]$ bands are marked in green, the asymmetric ones are marked in light blue (For interpretation of the references to color in this figure legend, the reader is referred to the web version of this article.).

At low coverage, bands appear at 1230 cm^{-1} and 1037 cm^{-1}. These bands are assigned to the $\nu(CF_3)_s$ and $\nu(SO_2)_s$ modes, respectively. Based on the MSSR rule, the observation of exclusively symmetrical bands indicates that the molecules adsorb at an upright position on the Pt(111) surface. This is consistent with previous studies on Au(111) [43]. With increasing coverage, bands form at 1564 cm^{-1}, 1452 cm^{-1}, and 1290 cm^{-1}, assigned to $\nu(N\text{-}C\text{-}N)_{as}$, $\delta(C\text{-}C)$ and $\nu(SO_2)_{as}$, respectively. At this point, asymmetric bands begin to grow, indicating less ordered growth. At higher coverage, another band can be observed at 1175 cm^{-1}, which is assigned to the $\nu(CF_3)_{as}$ mode. We note that the features from the cation are rather weak and it cannot be concluded from this data, whether the cation remains fully intact or undergoes some surface reaction.

At a sample temperature of 120 K (Fig. 6a), the IL bands appear in similar positions. Differences are found in the additional vibrations at 3162 cm^{-1}, 2986 cm^{-1}, 2947 cm^{-1} and 2925 cm^{-1}, which are assigned to $\nu(CH)$ vibrations of the imidazolium ring and the C_1 and C_2 side chains. Due to the lower surface temperature, it is expected that less well-ordered structures are formed at 120 K. Because of the lower degrees of ordering, the intensities of the asymmetric bands are higher and different $\nu(CH)$ modes are detectable.

3.6. Growth of $[C_2C_1Im][OTf]$ on DMA pre-covered Pt(111)

In order to study the influence of the IL on the DMA layer, we pre-covered the Pt(111) surface by exposure to 2 L DMA (see Fig. 7). Subsequently, we deposited the IL layer. During the deposition, time-resolved IRA spectra were recorded (similar to the experiments described in Section 3.5). Note that DMA was deposited before deposition the IL, because DMA did not adsorb on the IL-precovered surface (similar behavior was observed for other adsorbates such as CO where adsorption through a closed IL layer was not possible in UHV experiments [60]). From the spectroscopic point of view, pre-deposition of DMA is advantageous, since the IR bands from DMA are rather weak and, therefore, are easily masked by the IL. First, we evaluate the experiment at 120 K. Before deposition of the IL, we observe the bands of DMA at 2890 cm^{-1}, 2785 cm^{-1}, 1475 cm^{-1}, and 899 cm^{-1} (Fig. 7a, labelled in red). For the assignment, we refer to Section 3.1. At low coverage of $[C_2C_1Im][OTf]$, IL bands appear at 3117 cm^{-1}, 2927 cm^{-1}, 1577 cm^{-1}, 1524 cm^{-1}, 1471 cm^{-1}, 1280 cm^{-1}, 1232 cm^{-1}, 1175 cm^{-1} and 1037 cm^{-1}. We assign the bands at 3117 cm^{-1}, 2927 cm^{-1} and 1577 cm^{-1} to $\nu(CH)_{as}$ from the imidazolium ring, $\nu(CH)_{s+as}$ from the ethyl and methyl chain of $[C_2C_1Im]^+$ and $\nu(N\text{-}C\text{-}N)_{as}$, respectively. The band at 1524 cm^{-1} is neither visible in the spectra of $[C_2C_1Im][OTf]$ nor in the spectra of DMA deposited on Pt(111) without IL. We propose that an acid-base reaction occurs between the basic DMA and the slight acidic hydrogen at the C2 position the imidazolium ring. We tentatively attribute the band to a CN mode of the deprotonated imidazolium entity. For the vibration at 1471 cm^{-1}, the right shoulder can be assigned to the $\delta(C\text{-}C)$ vibration, and for the left shoulder we observe a $\delta(CH_3)$ vibration of the DMA. The $[OTf]^-$ bands at 1280 cm^{-1}, 1232 cm^{-1}, 1175 cm^{-1} and 1037 cm^{-1} are assigned to $\nu(SO_2)_{as}$, $\nu(CF_3)_s$, $\nu(CF_3)_{as}$ and $\nu(SO_2)_s$, respectively, according to the experiment described in Section 3.5. With increasing IL coverage, the DMA signals lose intensity. This could be due

to two reasons: First, the DMA is displaced by the IL. From previous studies, we know that even strong adsorbents, i.e., CO, are partially displaced by co-adsorbed IL [60,61] and that competition of adsorption sites leads to a lower binding energy of the adsorbents. However, the IL is not able to completely suppress the DMA signal. Secondly, reorientation could change the intensity ratio of the signals (MSSR rule), i.e. DMA could rearrange to a less space consuming geometry in order to allow co-adsorption with the IL [60].

At 300 K, we initially observe signals from MAC at 3402 cm^{-1}, 2918 cm^{-1}, 1488 cm^{-1}, 1402 cm^{-1} and 1297 cm^{-1} (see Section 3.2 for a detailed assignment). Upon deposition of the IL, bands appear at low coverage at 1421 cm^{-1}, 1232 cm^{-1}, 1175 cm^{-1}, and 1037 cm^{-1}, which are assigned to ν(N-C-N)$_{as}$, $\nu(CF_3)_s$, $\nu(CF_3)_{as}$ and $\nu(SO_2)_s$ modes, respectively. With increasing IL coverage, an additional signal grows at 1280 cm^{-1}, which is assigned to the $\nu(SO_2)_{as}$ mode. This behavior is similar to the effect of the experiment at low temperature. The increase of the intensity of the asymmetric bands indicated a loss of alignment of the $[OTf]^-$ species at higher coverage.

3.7. Influence of co-adsorbed DMA on the $[C_2C_1Im][OTf]$ layer

Next, we analyze the influence of the DMA and MAC on the $[C_2C_1Im][OTf]$ in more detail. To this aim, we plotted the spectra of $[C_2C_1Im][OTf]$ (black), $[C_2C_1Im][OTf]$ on DMA or MAC (red) and DMA or MAC without IL (green) both for adsorption at 120 K (top) and 300 K (bottom) in Fig. 8. For comparison, the spectra of DMA and MAC on $[C_2C_1Im][OTf]$ (red) and $[C_2C_1Im][OTf]$ (black) were scaled to the same height of the $\nu(SO_2)_s$ band.

In Fig. 8a, we focus on the differences in the spectral region from 1700 cm^{-1} to 1300 cm^{-1}. At 120 K and with pre-adsorbed DMA, the ν(N-C-N)$_{as}$ signal is more pronounced. At 1524 cm^{-1}, a band is formed at in the DMA+$[C_2C_1Im][OTf]$ measurement, which is not observed in either the DMA or the $[C_2C_1Im][OTf]$ spectra. As discussed in Section 3.6, we propose that this band results from an acid-base reaction between the acidic proton at the C2 position of the imidazolium ring and the basic DMA. For the surface pre-covered by MAC this band is not observed. The difference is rationalized by the lack of basicity of MAC. At 120 K, the δ(C-C) band at 1471 cm^{-1} overlaps with $\delta(CH_3)$ from DMA.

Next, we consider the spectra measured at 300 K. Similarly, we observe a stronger ν(N-C-N)$_{as}$ signal in co-adsorption (red). The $[C_2C_1Im]^+$ band δ(C-C) overlaps with the ν(N-C$_{ads}$) band from the MAC. The ν(CN) band for MAC at 1402 cm^{-1} is not visible for the co-adsorption. As MAC is influenced by the IL, it adopts in a different binding angle. We assume that MAC is no longer perpendicular. Since the CN band is aligned with the surface normal, the intensity is strongly influenced by angular changes (MSSR). Due to the influence of IL, the wavenumber also changes and we assume that the ν(CN) mode now overlaps with the IL band at 1420 cm^{-1}. Finally, we consider the $[OTf]^-$ region from 1350 cm^{-1} to 1000 cm^{-1} (Fig. 8b). While the symmetric bands of $\nu(CF_3)_s$ and $\nu(SO_2)_s$ hardly show any intensity changes due to the pre-adsorbed DMA/MAC, the asymmetric $\nu(CF_3)_{as}$ and $\nu(SO_2)_{as}$ bands increase in intensity due to the pre-adsorbed species. We attribute this effect to a change in the adsorption geometry because of the pre-adsorbed DMA/MAC. As Pt(111) sites are preoccupied the IL monolayer is completed faster and multilayer-like growth starts earlier leading to a more random molecular orientation. Because of the MSSR rule, the intensities of asymmetric bands are then more pronounced.

3.8. Thermal behavior and stability of $[C_2C_1Im][OTf]$ on Pt(111)

After studying the deposition, we now focus on the thermal behavior and reactivity of the deposited molecules. To this aim, we applied a

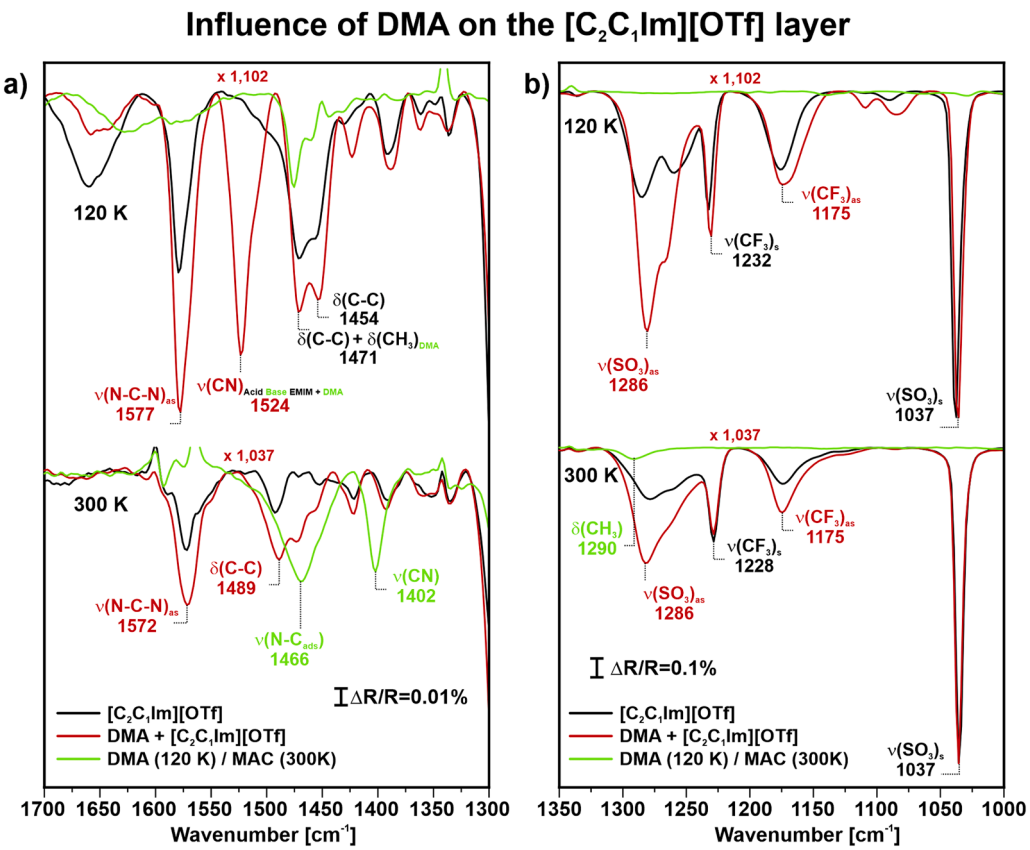

Fig. 8. Comparison of the $[C_2C_1Im][OTf]$ spectra (black) with the DMA + $[C_2C_1Im][OTf]$ spectra (red; normalized to the height of the $[C_2C_1Im][OTf]$ spectra at 1037 cm^{-1}) and the DMA/MAC spectra (green) in the (a) CN-region of the $[C_2C_1Im]^+$ cation and (b) $[OTf]^-$ anion region both at 120 K and 300 K (For interpretation of the references to color in this figure legend, the reader is referred to the web version of this article.).

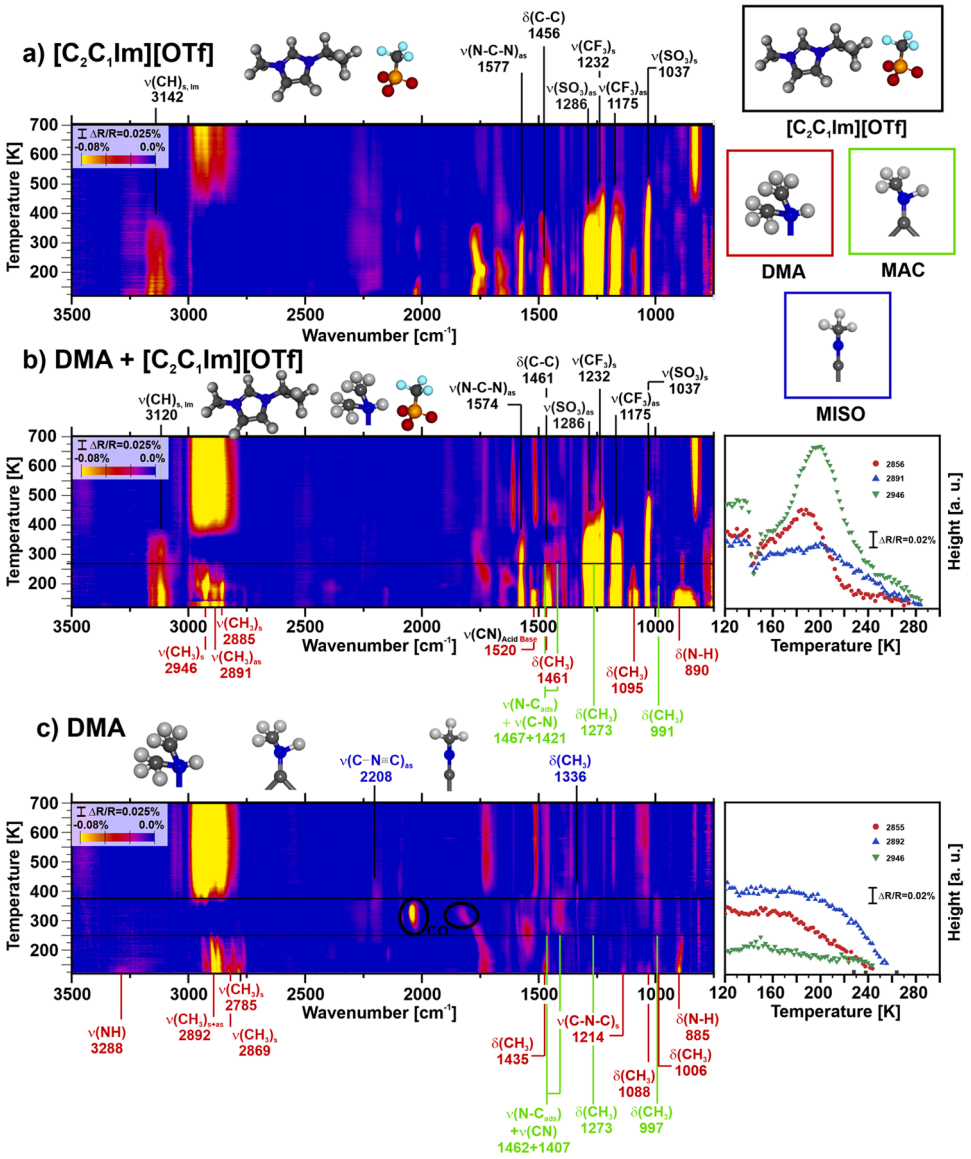

Fig. 9. Thermal stability and reactivity measured by temperature-programmed IRAS spectra (TP-IRAS) from 120 to 700 K; (a) $[C_2C_1Im][OTf]$ on Pt(111) with sketches of the molecules and their color code for the band assignment; (b) DMA + $[C_2C_1Im][OTf]$ on Pt(111) with an integration plot of the ν(CH) vibrations; (c) DMA on Pt(111) with an integration plot of the ν(CH) vibrations.

linear heating ramp of 2 K/min from 120 to 700 K and measured IRAS spectra every minute (see Experimental Section for details). Three sets of spectra were measured, i.e. $[C_2C_1Im][OTf]$ on Pt(111) (Fig. 9a), DMA on $[C_2C_1Im][OTf]$/Pt(111) SCILL (Fig. 9b), and DMA on Pt(111) (Fig. 9c).

First, we consider the thermal behavior and stability of the IL on Pt(111) after deposition of ~ 2 ML of $[C_2C_1Im][OTf]$ on Pt(111) (Fig. 9a). The asymmetric $[OTf]^-$ anion bands at 1286 cm^{-1} ($\nu(SO_2)_{as}$) and 1175 cm^{-1} ($\nu(CF_3)_{as}$) and the cation bands at 3142 cm^{-1}, 1577 cm^{-1}, 1456 cm^{-1} are visible until ~ 420 K. The symmetric $[OTf]^-$ bands at 1232 cm^{-1} ($\nu(CF_3)_s$) and 1037 cm^{-1} ($\nu(SO_2)_s$) even until ~ 500 K. This is consistent with the fact that anion derived species reside in the surface adopting an upright adsorption geometry. Above those temperatures, the intensity of the residual IL bands decreases indicating decomposition and desorption. Above ~ 500 K, no IL-derived bands can be observed.

3.9. Thermal behavior and reactivity of DMA on Pt(111)

Next, we investigated the behavior of DMA (~ 2 L) on clean Pt(111) by performing a TP-IRAS experiment with identical experimental parameters as used for IL experiment in Section 3.8. The corresponding data is shown in Fig. 9c. Up to ~ 245 K, bands assigned to DMA are observed (red). The signals of the ν(CH) vibration were integrated to determine the stability of DMA on Pt(111) (see Fig. 9c, right plot). At higher temperature, the DMA signals vanish and new signals appear at 2042 cm^{-1}, 1826 cm^{-1}, 1462 cm^{-1}, 1421 cm^{-1}, 1273 cm^{-1} and 997 cm^{-1}. The bands at 2042 cm^{-1} and 1826 cm^{-1} can be assigned to CO_{top} and CO_{bridge}, respectively, while the other signals can be assigned to MAC (green). As described by Mudiyanselage et al. [48], the transition from DMA to MAC leads to formation of empty adsorption sites available for adsorption of residual CO. In addition a small amount of CO is observed on bridging sites [48]. Above ~ 300 K, additional bands at 2208 cm^{-1} and 1336 cm^{-1} are observed (blue). Both bands can be assigned to MISO. Above 350 K, the MAC signals disappear and decomposition signals form. The MISO signals are present on the surface up to ~ 430 K.

3.10. Thermal behavior, stability, and reactivity of DMA on a [C_2C_1Im][OTf]/Pt(111) SCILL

Finally, we studied the dehydrogenation reaction of DMA on [C_2C_1Im][OTf] precovered Pt(111) (see Fig. 9b). We pre-adsorbed DMA on the Pt(111) sample and, subsequently, covered the film by exposure to ~ 2 ML of [C_2C_1Im][OTf]. Subsequently the same temperature programmed IR experiment was performed as described in Sections 3.8 and 3.9.

At up to 280 K, we observe bands at 3120 cm^{-1}, 1574 cm^{-1}, 1461 cm^{-1}, 1286 cm^{-1}, 1232 cm^{-1}, 1175 cm^{-1}, 1037 cm^{-1} and 852 cm^{-1}, which we attribute to [C_2C_1Im][OTf] (black). Additional bands at 2946 cm^{-1}, 2891 cm^{-1}, 2885 cm^{-1}, 1520 cm^{-1}, 1461 cm^{-1} and 890 cm^{-1} are attributed to the DMA (red). Because of the overlap of many DMA and IL bands, we again use the integrated area in the ν(CH) to follow the reaction and desorption of DMA (Fig. 9b, right plot). First, we notice an abrupt change of the intensity of the ν(CH) bands at ~ 130 K, which we assign to a reorientation of the DMA layer. The decrease of intensity of all DMA bands from ~ 180 K indicates the onset of the dehydrogenation or partial desorption of DMA. Here we already observe the formation of a weak band at 991 cm^{-1}, which indicated the formation of MAC. At higher temperature, other signals related to the formation of MAC (like 1467 cm^{-1} or 1421 cm^{-1}) become visible as well. Above ~ 280 K, all DMA related bands have disappeared completely. We notice that there is significant temperature difference in comparison to DMA dehydrogenation on pristine Pt(111), where DMA is present up to ~ 250 K only. We conclude the onset of DMA dehydrogenation is shifted by approximately 30 K in the presence of the IL. The effect could be explained as follows: First, the IL could stabilize the DMA on the surface. The stabilization effect could possibly result from the above discussed acid-base reaction with the DMA. Secondly, the IL is expected to block the addition sites required for the dehydrogenation reaction. Note that the dehydrogenation requires additional space for adsorption of the hydrogen and the rearrangement of the molecule, which adsorbs *via* a carbon atom after dehydrogenation. Both effects require additional space on the surface.

Above ~ 280 K, bands are observed at 1467 cm^{-1}, 1421 cm^{-1} and 991 cm^{-1}, which can be attributed to MAC. The MAC band at 1273 cm^{-1} is not visible as it directly overlaps with the $\nu(SO_2)_{as}$ and $\nu(CF_3)_s$ signals. The CO signals observed on pristine Pt(111) during MAC formation are not observed on the SCILL catalyst. Since CO would adsorb only on free Pt(111) sites, the IL most likely blocks these sites. Above ~ 380 K, all derived MAC disappear. At even higher temperatures, the IL desorbs or decomposes, similar as in the absence of the reactants.

4. Conclusions

In this work, we investigated the dehydrogenation reaction of DMA on a Pt-based model SCILL using DFT calculations and IRAS measurements. In particular, we investigated the deposition of [C_2C_1Im][OTf] and DMA, the mutual interaction of the co-adsorbates, and the dehydrogenation reaction of DMA on a pristine Pt(111) and in the presence of [C_2C_1Im][OTf]. The main conclusions are summarized as follows:

(1) *DMA growth on Pt(111):* At 120 K, DMA adsorbs molecularly *via* a lone electron pair of the nitrogen atom. The DMA adsorbs at an atop position in a tilted adsorption motif. At room temperature, the DMA partially dehydrogenates to MAC, which binds to Pt (111) *via* its carbon atom in bridge and hollow positions. At 400 K, further dehydrogenation to MISO takes place with the characteristic $\nu(C\text{-}N{\equiv}C)_{as}$ band appearing in the IR spectrum at 2197 cm^{-1}.

(2) *Influence of DMA on [C_2C_1Im][OTf] films:* Pre-adsorbed DMA competes with [C_2C_1Im][OTf] for the adsorption sites on the surface. In the presence of DMA/MAC, the IL adsorbs in a different geometry showing less alignment and a more random orientation of the $[OTf]^-$ anion.

(3) *Stability of DMA on Pt(111) and [C_2C_1Im][OTf]/Pt(111) SCILL:* The stability of DMA on pristine Pt(111) is lower than in the presence of the co-adsorbed IL film. This effect could be due either to stabilization of the DMA by co-adsorbed IL (e.g., due to proton transfer from the imidazolium to the DMA) or due to blocking of the reaction sites for dehydrogenation by the IL. In addition, the IL suppresses the co-adsorption of CO on the surface after partial dehydrogenation of DMA to MAC. Further dehydrogenation to MISO was not observed in the presence of the IL. These results suggest that the IL has a pronounced effect on the individual reaction steps of the dehydrogenation reaction, which in the case of competing reactions would give rise to changes of selectivity.

CRediT authorship contribution statement

Roman Eschenbacher: Investigation, Formal analysis, Data curation, Visualization, Writing – original draft. **Julien Steffen:** Software, Investigation, Data curation, Visualization, Writing – original draft. **Karl Farrugia:** Investigation. **Nicola Taccardi:** Investigation, Writing – review & editing. **Peter Wasserscheid:** Resources, Funding acquisition, Project administration, Supervision, Writing – review & editing. **Andreas Görling:** Conceptualization, Software, Resources, Funding acquisition, Project administration, Supervision, Writing – review & editing. **Jörg Libuda:** Conceptualization, Resources, Funding acquisition, Project administration, Supervision, Writing – review & editing.

Declaration of competing interest

The authors declare that they have no known competing financial interests or personal relationships that could have appeared to influence the work reported in this paper.

Data availability

The data that support the findings of this study are presented in the Manuscript. Source data are provided at Zenodo: https://zenodo.org/doi/10.5281/zenodo.10254227.

Acknowledgments

The authors declare no financial interest. This work was funded by the Deutsche Forschungsgemeinschaft (DFG, German Research Foundation) – Project-ID 431791331 – SFB 1452 (CLINT Catalysis at Liquid Interfaces). The authors acknowledge further support by the DFG *via* the projects 322419553 and 453560721. The authors gratefully acknowledge the scientific support and HPC resources provided by the Erlangen National High Performance Computing Center (NHR@FAU) of the Friedrich-Alexander-Universität Erlangen-Nürnberg (FAU) under the NHR project b146dc. NHR funding is provided by federal and Bavarian state authorities. NHR@FAU hardware is partially funded by the German Research Foundation (DFG) –440719683.

References

[1] U Kernchen, B Etzold, W Korth, A Jess, Solid Catalyst with Ionic Liquid Layer (SCILL) – A New Concept to Improve Selectivity Illustrated by Hydrogenation of Cyclooctadiene, Chem Eng & Technol 30 (2007) 985–994, https://doi.org/10.1002/ceat.200700050.

[2] H-P Steinrück, P Wasserscheid, Ionic Liquids in Catalysis, Catal Letters 145 (2015) 380–397, https://doi.org/10.1007/s10562-014-1435-x.

[3] T Bauer, S Mehl, O Brummel, et al., Ligand Effects at Ionic Liquid-Modified Interfaces: Coadsorption of [C2C1Im][OTf] and CO on Pd(111), J Phys Chem C 120 (2016) 4453–4465, https://doi.org/10.1021/acs.jpcc.6b00351.

[4] T Cremer, M Killian, JM Gottfried, et al., Physical Vapor Deposition of [EMIM][Tf_2N]: A New Approach to the Modification of Surface Properties with Ultrathin Ionic Liquid Films, ChemPhysChem 9 (2008) 2185–2190, https://doi.org/10.1002/cphc.200800300.

[5] T Barth, W Korth, A Jess, Selectivity-Enhancing Effect of a SCILL Catalyst in Butadiene Hydrogenation, Chem Eng & Technol 40 (2016) 395–404, https://doi.org/10.1002/ceat.201600140.

[6] C Meyer, V Hager, W Schwieger, P Wasserscheid, Enhanced activity and selectivity in n-octane isomerization using a bifunctional SCILL catalyst, J Catal 292 (2012) 157–165, https://doi.org/10.1016/j.jcat.2012.05.008.

[7] H-P Steinrück, J Libuda, P Wasserscheid, et al., Surface Science and Model Catalysis with Ionic Liquid-Modified Materials, Adv Mater 23 (2011) 2571–2587, https://doi.org/10.1002/adma.201100211.

[8] T Welton, Room-Temperature Ionic Liquids. Solvents for Synthesis and Catalysis, Chem Rev 99 (1999) 2071–2084, https://doi.org/10.1021/cr980032t.

[9] P Wasserscheid, W Keim, Ionic Liquids—New "Solutions" for Transition Metal Catalysis, Angew Chemie 39 (2000) 3772–3789, https://doi.org/10.1002/1521-3773(20001103)39:21<3772::aid-anie3772>3.0.co;2-5.

[10] IT Horváth, J Rábai, Facile Catalyst Separation Without Water: Fluorous Biphase Hydroformylation of Olefins, Science 266 (1994) 72–75, https://doi.org/10.1126/science.266.5182.72, 80-.

[11] JS Wilkes, A short history of ionic liquids—from molten salts to neoteric solvents, Green Chem 4 (2002) 73–80, https://doi.org/10.1039/b110838g.

[12] C Meyer, S Werner, M Haumann, P Wasserscheid, Chemical Engineering of Ionic Liquid Processes, in: N V Plechkova, R Seddon Kenneth (Eds.), Ionic Liquids Completely UnCOILed: Critical Expert Overviews, John Wiley & Sons, Inc, Hoboken, NJ, 2015, pp. 107–144.

[13] U Kernchen, B Etzold, W Korth, A Jess, Solid catalyst ionic liquid layer (SCILL) - A new concept to improve selectivity illustrated by hydrogenation of cyclooctadiene, Chem Eng Technol 30 (2007) 985–994, https://doi.org/10.1002/ceat.200700050.

[14] N Yao, HB Wang, YL Hu, Recent Progress on Electrochemical Application of Room-Temperature Ionic Liquids, Mini Rev Org Chem 14 (2017) 237–254, https://doi.org/10.2174/1570193X14666170420115644.

[15] T Boldoo, M Lee, H Cho, Enhancing the solar energy conversion and harvesting characteristics of multiwalled carbon nanotubes-modified 1-hexyl-3-methyl-imidazolium cation ionic liquids, Int J ENERGY Res 46 (2022) 8891–8907, https://doi.org/10.1002/er.7763.

[16] YH Hu, HY Xiao, L Fu, et al., Confined Ionic-Liquid-Mediated Cation Diffusion through Layered Membranes for High-Performance Osmotic Energy Conversion, Adv Mater (2023), https://doi.org/10.1002/adma.202301285.

[17] G Choudhary, J Dhariwal, M Saha, et al., Ionic liquids: environmentally sustainable materials for energy conversion and storage applications, Environ Sci Pollut Res (2023), https://doi.org/10.1007/s11356-023-25468-w.

[18] Z Rahman, SK Das, Ionic-Liquid-Based, Sustainable Wavelength-Shifting Materials for Energy Conversion: A Minireview, CHEMISTRYSELECT 7 (2022), https://doi.org/10.1002/slct.202103898.

[19] TA Pham, Ab initio simulations of liquid electrolytes for energy conversion and storage, Int J Quantum Chem 119 (2019), https://doi.org/10.1002/qua.25795.

[20] TJ Abraham, DR MacFarlane, RH Baughman, et al., Towards ionic liquid-based thermoelectrochemical cells for the harvesting of thermal energy, Electrochim Acta 113 (2013) 87–93, https://doi.org/10.1016/j.electacta.2013.08.087.

[21] CR Feng, CPH Rajapaksha, A Jakli, Ionic Elastomers for Electric Actuators and Sensors, ENGINEERING 7 (2021) 581–602, https://doi.org/10.1016/j.eng.2021.02.014.

[22] CH Zhang, B He, ZP Wang, et al., Application and Analysis of an Ionic Liquid Gel in a Soft Robot, Adv Mater Sci Eng 2019 (2019), https://doi.org/10.1155/2019/2857282.

[23] JJ Wang, Innovating ionic liquids as repairable electronics for liquid robots, GREEN ENERGY Environ 5 (2020) 122–123, https://doi.org/10.1016/j.gee.2020.04.005.

[24] T Bauer, V Hager, MB Williams, et al., Palladium-Mediated Ethylation of the Imidazolium Cation Monitored In Operando on a Solid Catalyst with Ionic Liquid Layer, ChemCatChem 9 (2016) 109–113, https://doi.org/10.1002/cctc.201601222.

[25] N Szesni, R Fischer, A Hagemeyer, et al., Catalyst composition for selective hydrogenation with improved characteristics, 2013. U.S. Patent WO2013057244A1.

[26] J Arras, M Steffan, Y Shayeghi, P Claus, The promoting effect of a dicyanamide based ionic liquid in the selective hydrogenation of citral, Chem Commun (2008) 4058–4060, https://doi.org/10.1039/b810291k.

[27] J Arras, M Steffan, Y Shayeghi, et al., Regioselective catalytic hydrogenation of citral with ionic liquids as reaction modifiers, Green Chem 11 (2009) 716, https://doi.org/10.1039/b822992a.

[28] J Arras, E Paki, C Roth, et al., How a Supported Metal Is Influenced by an Ionic Liquid: In-Depth Characterization of SCILL-Type Palladium Catalysts and Their Hydrogen Adsorption, J Phys Chem C 114 (2010) 10520–10526, https://doi.org/10.1021/jp1016196.

[29] F Maier, T Cremer, C Kolbeck, et al., Insights into the surface composition and enrichment effects of ionic liquids and ionic liquid mixtures, Phys Chem Chem Phys 12 (2010) 1905, https://doi.org/10.1039/b920804f.

[30] H-P Steinrück, Surface science goes liquid !, Surf Sci 604 (2010) 481–484, https://doi.org/10.1016/j.susc.2009.12.033.

[31] P Wasserscheid, Volatile times for ionic liquids, Nature 439 (2006) 797, https://doi.org/10.1038/439797a.

[32] JP Leal, JMSS Esperança, ME Minas da Piedade, et al., The Nature of Ionic Liquids in the Gas Phase, J Phys Chem A 111 (2007) 6176–6182, https://doi.org/10.1021/jp073006k.

[33] JP Armstrong, C Hurst, RG Jones, et al., Vapourisation of ionic liquids, Phys Chem Chem Phys 9 (2007) 982, https://doi.org/10.1039/b615137j.

[34] KRJ Lovelock, IJ Villar-Garcia, F Maier, et al., Photoelectron Spectroscopy of Ionic Liquid-Based Interfaces, Chem Rev 110 (2010) 5158–5190, https://doi.org/10.1021/cr100114t.

[35] T Cremer, L Wibmer, SK Calderón, et al., Interfaces of ionic liquids and transition metal surfaces—adsorption, growth, and thermal reactions of ultrathin [C1C1Im][Tf2N] films on metallic and oxidised Ni(111) surfaces, Phys Chem Chem Phys 14 (2012) 5153, https://doi.org/10.1039/c2cp40278e.

[36] T Xu, T Wähler, J Vecchietti, et al., Interaction of Ester-Functionalized Ionic Liquids with Atomically-Defined Cobalt Oxides Surfaces: Adsorption, Reaction and Thermal Stability, ChemPhysChem 18 (2017) 3443–3453, https://doi.org/10.1002/cphc.201700843.

[37] M Sobota, I Nikiforidis, W Hieringer, et al., Toward Ionic-Liquid-Based Model Catalysis: Growth, Orientation, Conformation, and Interaction Mechanism of the [Tf 2 N] – Anion in [BMIM][Tf 2 N] Thin Films on a Well-Ordered Alumina Surface, Langmuir 26 (2010) 7199–7207, https://doi.org/10.1021/la904319h.

[38] MF Friedrich, M Lucas, P Claus, Selective hydrogenation of propyne on a solid Pd/Al2O3 catalyst modified with ionic liquid layer (SCILL), Catal Commun 88 (2017) 73–76, https://doi.org/10.1016/j.catcom.2016.09.036.

[39] L Naicker, M Schoerner, D Kremitzl, et al., Influencing the Product Distribution in Citral Hydrogenation Using Ionic Liquid Modified Cu Catalysts, ChemCatChem 14 (2022), https://doi.org/10.1002/cctc.202200388.

[40] R Hou, X Lan, T Wang, Selective hydrogenation of acetylene on Pd/SiO2 in bulk liquid phase: A comparison with solid catalyst with ionic liquid layer (SCILL), Catal TODAY 251 (2015) 47–52, https://doi.org/10.1016/j.cattod.2014.09.006.

[41] R Chanerika, ML Shozi, M Prato, HB Friedrich, The Effect of Coating Pd/Al2O3 and PdAg/Al2O3 Catalysts with {[}BMIM]{[}DCA] for the Selective Hydrogenation of 1-Octyne in 1-Octene, ChemCatChem (2022), https://doi.org/10.1002/cctc.202201043.

[42] Schernich S, Wagner V, Taccardi N, et al (2014) Interface Controls Spontaneous Crystallization in Thin Films of the Ionic Liquid [C 2 C 1 Im][OTf] on Atomically Clean Pd(111). 30:6851. https://doi.org/10.1021/la500842c.

[43] H Bühlmeyer, J Hauner, R Eschenbacher, et al., Structure Formation in an Ionic Liquid Wetting Layer: A Combined STM, IRAS, DFT and MD Study of [C2C1Im][OTf] on Au(111), Chem - A Eur J 29 (2023) e202301328, https://doi.org/10.1002/chem.202301328.

[44] S Schernich, D Kostyshyn, V Wagner, et al., Interactions Between the Room-Temperature Ionic Liquid [C2C1Im][OTf] and Pd(111), Well-Ordered Al2O3, and Supported Pd Model Catalysts from IR Spectroscopy, J Phys Chem C 118 (2014) 3188–3193, https://doi.org/10.1021/jp5006692.

[45] O Brummel, F Faisal, T Bauer, et al., Ionic Liquid-Modified Electrocatalysts: The Interaction of [C1C2Im][OTf] with Pt(111) and its Influence on Methanol Oxidation Studied by Electrochemical IR Spectroscopy, Electrochim Acta 188 (2016) 825–836, https://doi.org/10.1016/j.electacta.2015.12.006.

[46] T Yang, J Yang, X Deng, et al., Modifying the Electrocatalytic Selectivity of Oxidation Reactions with Ionic Liquids, Angew Chemie Int Ed 61 (2022) e202202957, https://doi.org/10.1002/anie.202202957.

[47] DH Kang, M Trenary, Surface chemistry of dimethylamine on Pt(1 1 1): Formation of methylaminocarbyne and its decomposition products, Surf Sci 519 (2002) 40–56, https://doi.org/10.1016/S0039-6028(02)02145-3.

[48] K Mudiyanselage, M Trenary, RJ Meyer, Formation of methyl isocyanide from dimethylamine on Pt(111), J Phys Chem C 112 (2008) 3794–3799, https://doi.org/10.1021/jp709581j.

[49] C Schuschke, C Hohner, M Jevric, et al., Solar energy storage at an atomically defined organic-oxide hybrid interface, Nat Commun 10 (2019), https://doi.org/10.1038/s41467-019-10263-4.

[50] G Kresse, J Furthmüller, Efficient iterative schemes for ab initio total-energy calculations using a plane-wave basis set, Phys Rev B 54 (1996) 11169–11186, https://doi.org/10.1103/PhysRevB.54.11169.

[51] G Kresse, J Furthmüller, Efficiency of ab-initio total energy calculations for metals and semiconductors using a plane-wave basis set, Comput Mater Sci 6 (1996) 15–50, https://doi.org/10.1016/0927-0256(96)00008-0.

[52] G Kresse, D Joubert, From ultrasoft pseudopotentials to the projector augmented-wave method, Phys Rev B 59 (1999) 1758–1775, https://doi.org/10.1103/PhysRevB.59.1758.

[53] JP Perdew, K Burke, M Ernzerhof, Generalized gradient approximation made simple, Phys Rev Lett 77 (1996) 3865–3868, https://doi.org/10.1103/PhysRevLett.77.3865.

[54] S Grimme, J Antony, S Ehrlich, H Krieg, A consistent and accurate ab initio parametrization of density functional dispersion correction (DFT-D) for the 94 elements H-Pu, J Chem Phys 132 (2010), https://doi.org/10.1063/1.3382344.

[55] S Grimme, S Ehrlich, L Goerigk, Effect of the damping function in dispersion corrected density functional theory, J Comput Chem 32 (2011) 1456–1465, https://doi.org/10.1002/jcc.21759.

[56] M Methfessel, AT Paxton, High-precision sampling for Brillouin-zone integration in metals, Phys Rev B 40 (1989) 3616–3621, https://doi.org/10.1103/PhysRevB.40.3616.

[57] FM Hoffmann, Infrared Reflection-Absorption Spectroscopy of Adsorbed Molecules, Surf Sci Rep 3 (1983) 107109–107192.

[58] C Schuschke, L Fromm, J Träg, et al., A Molecular View of the Ionic Liquid Catalyst Interface of SCILLs: Coverage-Dependent Adsorption Motifs of [C4C1Pyr][NTf2]

on Pd Single Crystals and Nanoparticles, J Phys Chem C 125 (2021) 13264–13272, https://doi.org/10.1021/acs.jpcc.1c02131.
[59] D Blaumeiser, C Schuschke, L Fromm, et al., CO Permeability and Wetting Behavior of Ionic Liquids on Pt(111): An IRAS and PM-IRAS Study from Ultrahigh Vacuum to Ambient Pressure, J Phys Chem C 125 (2021) 15301–15315, https://doi.org/10.1021/ACS.JPCC.1C04043/SUPPL_FILE/JP1C04043_SI_001.PDF.
[60] Eschenbacher R, Trzeciak S, Schuschke, Christian Schötz S, et al (2023) Thermal stability and CO permeability of [C4C1Pyr][NTf2]-based Pd Model SCILLs: From UHV to ambient pressure. Top Catal.
[61] R Eschenbacher, C Schuschke, H Bühlmeyer, et al., Interaction between Ionic Liquids and a Pt(111) Surface Probed by Coadsorbed CO as a Test Molecule, J Phys Chem Lett 12 (2021) 10079–10085, https://doi.org/10.1021/acs.jpclett.1c02983.
[62] M Sobota, M Happel, M Amende, et al., Ligand Effects in SCILL Model Systems: Site-Specific Interactions with Pt and Pd Nanoparticles, Adv Mater 23 (2011) 2617–2621, https://doi.org/10.1002/adma.201004064.
[63] C Schuschke, C Hohner, C Stumm, et al., Dynamic CO Adsorption and Desorption through the Ionic Liquid Layer of a Pt Model Solid Catalyst with Ionic Liquid Layers, J Phys Chem C 123 (2019) 31057–31072, https://doi.org/10.1021/acs.jpcc.9b09128.